

Lightwave topology for strong-field valleytronics

Á. Jiménez-Galán¹, R. E. F. Silva^{1,2}, O. Smirnova^{1,3}, & M. Ivanov^{1,4,5}

¹*Max-Born-Institute, Berlin, Germany.*

²*Department of Theoretical Condensed Matter Physics, Universidad Autónoma de Madrid, Spain*

³*Technische Universität Berlin, Berlin, Germany.*

⁴*Department of Physics, Humboldt University, Berlin, Germany.*

⁵*Blackett Laboratory, Imperial College London, London, United Kingdom.*

Modern light generation technology offers extraordinary capabilities for sculpting light pulses, with full control over individual electric field oscillations within each laser cycle ¹⁻³. These capabilities are at the core of lightwave electronics ⁴⁻⁸ – the dream of ultrafast lightwave control over electron dynamics in solids, on a few-cycle to sub-cycle timescale, aiming at information processing at tera-Hertz to peta-Hertz rates. Here we show a robust and general approach to ultrafast, valley-selective electron excitations in two-dimensional materials ⁹, by controlling the sub-cycle structure of non-resonant driving fields at a few-femtosecond timescale. Bringing the frequency-domain concept of topological Floquet systems ^{10,11} to the few-femtosecond time domain, we develop a transparent control mechanism in real space and an all-optical, non-element-specific method to coherently write, manipulate and read selective valley excitations using fields carried in a wide range of frequencies, on timescales orders of magnitude shorter than valley lifetime, crucial for implementation of valleytronic devices ¹².

Two-dimensional graphene-like systems with broken inversion symmetry, such as monolayer hexagonal boron nitride (hBN) or transition metal dichalcogenides (TMDs), are candidates for next generation quantum materials due to their high carrier mobility and, especially, to their valley degree of freedom⁹, with potential applications in quantum information processing. Valleys are local minima in the crystal band structure corresponding to different crystal momenta; in 2D hexagonal lattices they are located at the \mathbf{K} and $\mathbf{K}' = -\mathbf{K}$ points of the Brillouin zone (Fig. 1a). Selective excitation of \mathbf{K} or \mathbf{K}' can be achieved using weak circularly polarized field resonant with the direct band gap of the material¹³: it couples to either \mathbf{K} or \mathbf{K}' depending on light's helicity (the optical valley selection rule^{14,15}).

However, such weak fields pose a challenge for switching the generated excitations at the ultrafast time-scales, desirable due to short valley lifetimes¹² ($\sim 10^3 - 10^6$ fsec for excitons and electrons, respectively). A major step towards meeting this challenge has been made recently¹⁶: switching of the population between the \mathbf{K} and \mathbf{K}' valleys was achieved using the combination of a resonant pump pulse, which populated the desired valley, and a strong terahertz pulse, which moved the excited population within the Brillouin zone by controlling the THz field strength¹⁶.

The feasibility of applying strong non-resonant fields to bulk dielectrics^{7,17-19} and ultrathin transition metal dichalcogenide (TMD) films without material damage²⁰ opens major new opportunities in valleytronics. Our approach capitalizes on them. In contrast to previous work¹⁶, we require neither resonant light, nor the precise tuning of the strength of the control field. Instead, we use far off-resonant light to modify the topological properties of the system by inducing

Haldane-type ²¹ complex-valued second neighbour hoppings in a topologically-trivial lattice. This is done by using the bicircular light field composed of counter-rotating fundamental and its second harmonic. We find that rotating the Lissajous figure drawn by the electric field vector of such pulse (Fig. 1b), relative to the lattice (Fig. 1c), controls the magnitude and the phase of the complex light-induced second-neighbour hoppings, thus controlling the cycle-averaged band structure (Fig. 1d) and the Berry curvature in each valley. Exponential sensitivity of multi-photon excitation to the effective bandgap naturally leads to selective excitation in the valley where the bandgap is reduced. Thus, valley selection is achieved by tailoring the symmetry of the Lissajous figure to the lattice and controlling its orientation.

Using light to control topological properties of solids has led to the concept of topological Floquet lattices ^{10,11,22}. In this context, in addition to providing a real-space description of the effect, our key results are as follows. First, we find that strong low-frequency circularly polarized fields show opposite valley polarization than those in the weak-field, one-photon resonant regime, as a consequence of light-induced streaking of the excited electrons. Second, we initialize and manipulate valley polarization on a few femtosecond time scale in a way that remains consistent for a broad range of frequencies and field intensities, and independent of the specifics of the material. We give two examples, hexagonal boron nitride (hBN) and MoS₂. Third, using an additional linearly polarized probe pulse, we map the valley pseudospin onto the polarization of its harmonics, providing an all-optical measure of the valley asymmetry. Finally, we show numerical evidence of a topological phase transition induced by non-resonant, tailored light, occurring at specific values of intensity and wavelength of the driving field, just as predicted by our analytical model.

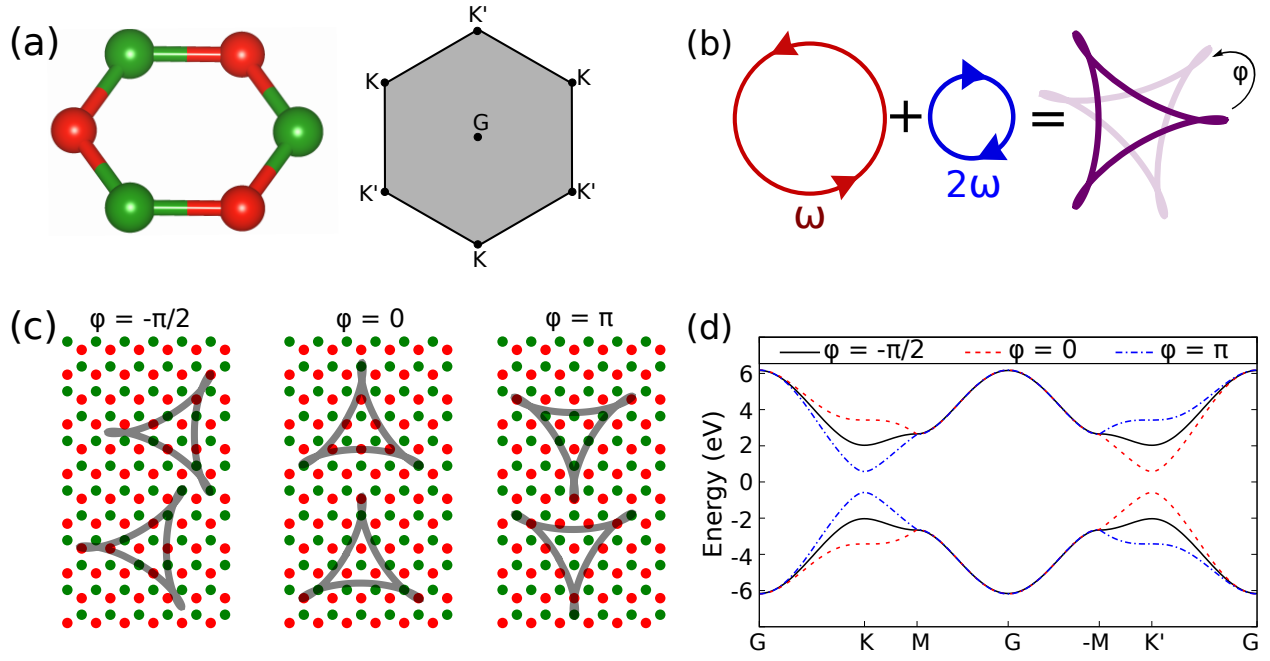


Figure 1: **Light-induced modification of the band structure with tailored field.** (a) 2D hexagonal lattice with broken inversion symmetry in real space (left; red and green represent two different atoms) and reciprocal space, with valleys K and K' (right). (b) The trefoil Lissajous figure generated by the field has the symmetry of the sub-lattice and can be rotated by changing the two-color phase φ . (c) Depending on the field orientation (grey trefoil), the two atomic sites are addressed differently. For $\varphi = -\pi/2$, the field interacts with both atoms equally and the bands show valley-degeneracy (d, black solid line). For $\varphi = 0$, the field interacts with the two types of atoms differently (note how the two atoms inside the trefoil are now not interchangeable, irrespective of where the field is placed in the lattice). This lifts the valley degeneracy (d, red dashed line). For $\varphi = \pi$, the situation is reversed (d, blue dashed dotted line).

Consider first strong circularly polarized fields with frequencies well below the band gap energy. In Fig. 2a,b,c we show the electron populations in the p_z conduction band of hBN after applying a strong ($I = 5 \text{ TW/cm}^2$) circularly polarized field with three different frequencies ω and the same helicity. The same observable can be obtained, e.g., by angularly-resolved photoemission spectroscopy (ARPES). The most excited valley switches as we transition from the highest frequency (Fig. 2a) to the lowest frequency (Fig. 2c). All panels switch \mathbf{K} for \mathbf{K}' when the helicity of the laser is reversed (See Supplementary Note 1).

This switch in valley polarization is a consequence of streaking: the rotation of the field selects excitation at the \mathbf{K} valley, as in the one-photon case, while the large magnitude of the vector potential ($A_0 = \sqrt{I}/\omega \simeq 0.8 \text{ a.u.}$) displaces the electron population towards the \mathbf{K}' valley. Thus, one can control valley polarization using non-resonant, low-frequency fields and controlling the field helicity. However, just like in one-photon resonant fields, the result is material specific and depends crucially on the relation between the band gap and the field frequency (Fig. 2a,b,c).

A robust approach is offered by a field widely used for controlling strong-field processes in atoms^{2,23,24}, which combines circularly polarized fundamental ω with its counter-rotating second harmonic:

$$\mathbf{F}_L = \hat{\mathbf{x}} [-F_1 \cos(\omega t) + F_2 \cos(2\omega t + \varphi)] + \hat{\mathbf{y}} [F_1 \sin(\omega t) + F_2 \sin(2\omega t + \varphi)], \quad (1)$$

where F_1 and F_2 are the field strengths of the fundamental and second harmonic respectively, φ is the sub-cycle phase delay between the two drivers. During one cycle, the field draws the trefoil shown in Fig 1b, which fits ideally the geometry of two triangular sub-lattices and can break

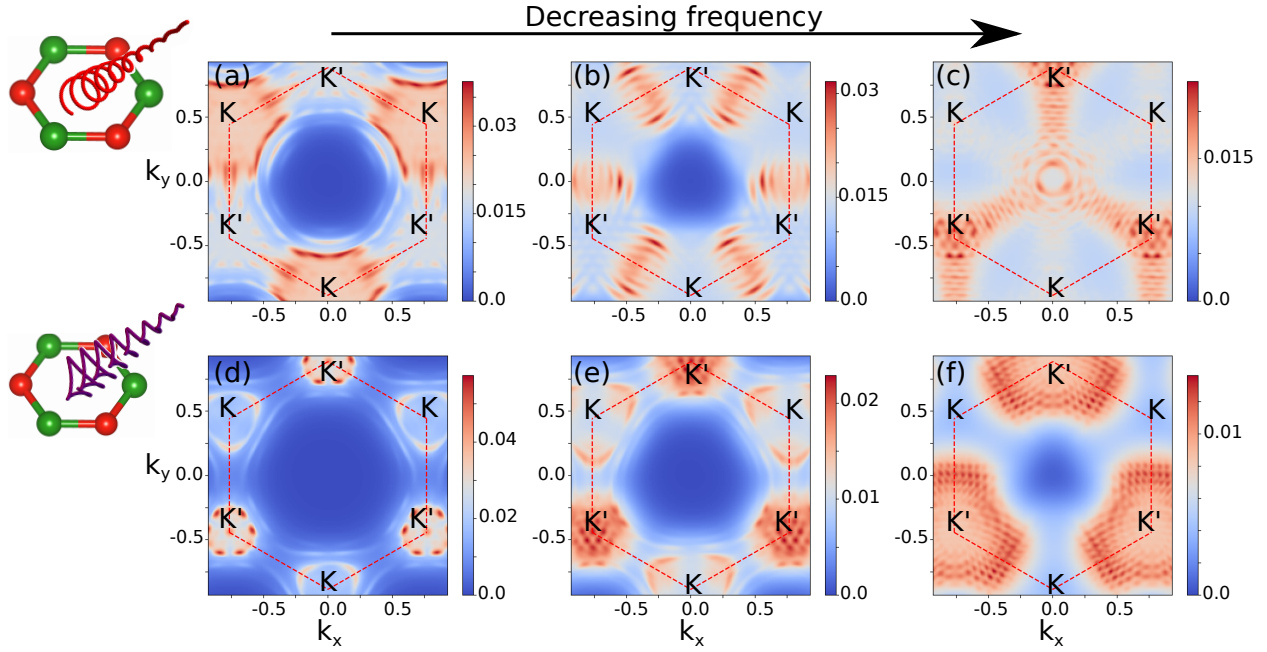


Figure 2: **Selective valley excitation in strong fields.** (a-c) Populations in the first Brillouin zone (red dashed hexagon) of the conduction band of monolayer hBN (band gap of $\Delta = 5.9$ eV) after applying a strong, circularly polarized pulse with frequencies: (a) $\omega = 0.95$ eV, (b) $\omega = 0.68$ eV and (c) $\omega = 0.41$ eV. All other parameters (helicity, peak field strength $F_L = 0.012$ a.u. and duration $\tau = 200$ fs) remain fixed. Valley selection changes in the low-frequency regime; all panels switch **K** for **K'** when the helicity is reversed (not shown). Panels (d-f) show the same for a bicircular field with the same F_L , τ and fundamental frequency ω as in the corresponding panels (a-c) above. The most populated valley now remains the same; reversing the overall helicity of the fields does not switch **K** to **K'** (not shown), indicating new robust mechanism for valley polarization.

the symmetry between these two identical sub-lattices in graphene inducing charge oscillations between them²⁵. Its orientation relative to the sublattices is controlled by φ .

Fig. 2d,e,f shows the valley polarization in hBN at fixed φ , for three different frequencies. In contrast to (a-c), now the most populated valley remains robust as we transition from the few-photon to the deep multiphoton regime (Fig. 2d,e,f). It is selected by the orientation of the trefoil relative to the lattice. The feasibility of changing the trefoil orientation during the pulse implies the ability to switch the valley pseudospin on the fly. Reversing the helicity of the two drivers (ω and 2ω) does not switch the valley polarization (see Supplementary Note 1), suggesting a new, robust mechanism for valley selection.

As shown in the Methods section, energy conserving processes involving both $2\hbar\omega$ and $\hbar\omega$ photons, such as absorption of one $2\hbar\omega$ photon and re-emission of two $\hbar\omega$ photons, lead to complex second-neighbour hopping t_2 . Its amplitude and phase are controlled by the field strengths and the two-color phase φ . A non-zero imaginary part lifts the valley degeneracy. For moderately strong fields (see Methods), the cycle-averaged, the imaginary component of laser-induced second neighbour hopping is

$$\mathcal{I}\{t_2\} \sim 2J_2\left(\frac{\sqrt{3}a_0 F_1}{\omega}\right) J_1\left(\frac{\sqrt{3}a_0 F_2}{2\omega}\right) \cos\varphi, \quad (2)$$

where a_0 is the lattice constant and J_n is the Bessel function of the first kind of order n . Thus, the sub-cycle control over the field geometry, φ , controls the topological properties of the dressed system. The associated modification of the band structure leads to the valley asymmetry, controlled by the two-color delay φ in a way that is not material specific.

To illustrate this, we consider monolayer hBN (see Methods for numerical details) and use a bicircular pulse with fundamental frequency $\omega = 0.41$ eV ($\lambda = 3000$ nm), duration of $\tau = 200$ fs, intensity ratio of $I(\omega)/I(2\omega) = 4$, and maximum peak intensity of $I = 5$ TW/cm² (lower than its predicted damage threshold ²⁶). We change the two-color phase φ to control the orientation of the field with respect to the lattice. The valley population asymmetry is calculated as $\mathcal{A} = \pm 2(f_{n,K} - f_{n,K'})/(f_{n,K} + f_{n,K'})$, where $f_{n,K}$ ($f_{n,K'}$) is obtained by integrating the electron population inside the black dashed circles encircling **K** (**K'**) in (a-c,e-g), and the + (−) sign is used for hBN (MoS₂), due to their opposite Berry curvatures.

When $\varphi = -\pi/2$, both sub-lattices are addressed equally, no valley asymmetry is present in the cycle-averaged band structures (Fig. 3a). We find that **K** and **K'** valleys of the conduction band are nearly equally excited. In contrast, when $\varphi = 0$, the cycle-averaged band structure shows a strong valley asymmetry (Fig. 3b). This reflects in the valley populations, which show a 60% contrast (Fig. 3d). The situation is reversed for $\varphi = \pi$, the populations switch to the opposite valley (Fig. 3c). The sense of rotation of the pulse also contributes to the valley asymmetry due to the orbital propensity rule, but its effect is relatively weak. It manifests in small valley polarization for $\varphi = \pm\pi/2$, and in that $\varphi = 0$ and $\varphi = \pi$ are not exact opposites (compare Figs. 3b,c).

To confirm that the mechanism is general, we performed calculations in MoS₂ for the same laser frequencies, which allows us to maintain the same timescale of valley control. Due to the smaller band gap of MoS₂, the intensity peak of the total field was kept at $I = 0.15$ TW/cm², well below its damage threshold ²⁰. Fig. 3(e)-(g) shows valley excitation after the pulse in the

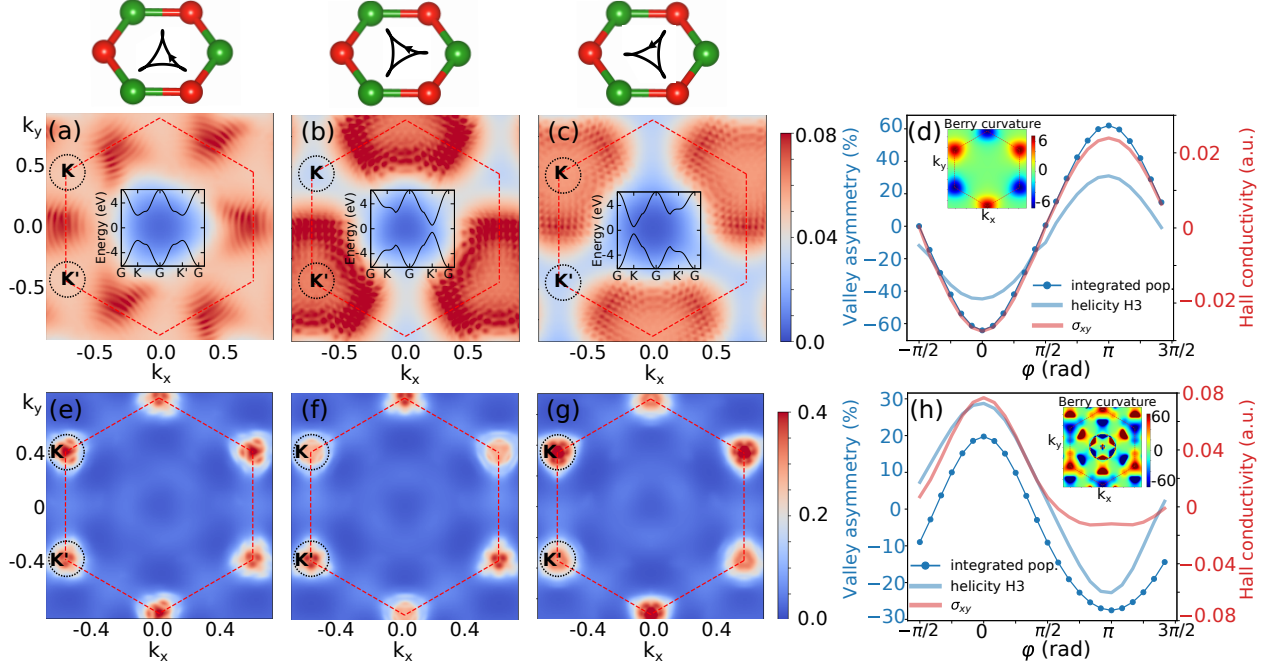


Figure 3: Strong-field manipulation and optical reading of valley polarization. Electron populations in the lowest conduction bands of hBN (a-c) and spin-integrated MoS₂ (e-g), after applying a bicircular field with $\lambda = 3\mu\text{m}$: (a,e) $\varphi = -\pi/2$, (b,f) $\varphi = 0$, and (c,g) $\varphi = \pi$, sketches of field orientations relative to the hexagonal cell are also shown. The insets in panels (a)-(c) show the cycle-averaged band structures for hBN (see Methods) vs φ . (d,h) Valley population asymmetry (dotted solid blue curve), helicity of the third harmonic of the probe (faint blue curve) and anomalous Hall conductivity (faint red curve), as a function of φ in (d) hBN and (h) MoS₂. The probe is carried at 3ω for hBN and ω for MoS₂; ω is the fundamental frequency of the bicircular pulse.

spin-integrated lowest conduction band of MoS₂ (see Supplementary Note 2 for spin-resolved results), illustrating similar control as for hBN, but with lower values of the valley polarization. Higher values of valley polarization can be obtained by increasing the field strength, while total populations can be controlled with the pulse duration.

We now turn to optical reading of the valley pseudospin. Since the Berry curvature is opposite at the **K** and **K'** valleys, when an in-plane electric field is applied, the carriers generate a current perpendicular to the electric field (anomalous current), with opposite direction at each valley. For equal valley populations, the anomalous current will thus cancel, leading to a zero anomalous Hall conductivity (AHC),

$$\sigma_{xy} = -\frac{e}{\hbar} \sum_n \int_{\text{BZ}} \frac{d\mathbf{k}}{(2\pi)^3} f_n(\mathbf{k}) \Omega_{n,z}(\mathbf{k}), \quad (3)$$

where f_n and Ω_n are the population and Berry curvature of the n -th band. If the valley populations are not equal, the perpendicular currents originating from **K** and **K'** do not compensate each other, leading to a non-zero AHC¹⁵. This so-called valley Hall effect has been demonstrated for MoS₂ monolayers by measuring the direction of the transverse Hall voltage²⁷.

Alternatively, the direction of the anomalous current can be retrieved all-optically from the helicity of the harmonics of a linearly polarized probe²⁸. To this end, we apply a probe field with frequency ω or 3ω , linearly polarized along the **G-M** direction of the lattice, and monitor the harmonic response at a $3N$ multiple of the probe frequency. This guarantees a background-free measurement without interference from harmonics generated by the bi-circular field, since the latter does not generate $3N\omega$ harmonics due to symmetry. The probe pulse arrives after the end of

the bicircular pump.

The component of the optical response polarized orthogonal to the probe polarization undergoes a phase jump of π as the population switches from one valley to another (see Methods), leading to a rotation in the helicity of the probe response, Fig. 3(d,h). The helicity is calculated as $h = 2(I_{\odot} - I_{\ominus})/(I_{\odot} + I_{\ominus})$, where I_{\odot} (I_{\ominus}) is the component of the harmonic intensity rotating clockwise (anticlockwise).

When the dynamics occur mainly in one conduction band, as in monolayer hBN, the helicity of the optical response reads the AHC and, consequently, the valley polarization (Fig. 3d). In the case of MoS₂ (Fig. 3h), the helicity follows the valley polarization qualitatively, but deviates from the AHC due to the influence of higher bands.

Our approximate analytical model for an effective t_2 Eq.(2) predicts a topological phase transition. To explore this prediction, we monitor the time-dependent anomalous Hall conductivity (AHC) in hBN during the laser pulse. Fig. 4 shows the gated time-dependent AHC defined as

$$\bar{\sigma}_{xy}(t) = \int_{-\infty}^{\infty} \sigma_{xy}(t') G(t' - t) dt', \quad (4)$$

where $\sigma_{xy}(t')$ is the instantaneous AHC, defined by Eq. 3 using instantaneous electron populations $f_n(\mathbf{k}, t)$. The instantaneous AHC is averaged over several laser cycles using the gate function $G(t' - t) = e^{-4 \ln 2 (t' - t)^2 / T^2}$, $T = 4 \times 2\pi / \omega$, to produce $\bar{\sigma}_{xy}(t)$.

Note that $\sigma_{xy}(t)$ uses field-free Berry curvature $\Omega(\mathbf{k})$ and field-free bands, for which $f_n(\mathbf{k}, t)$ are computed. Strikingly, we find that $\bar{\sigma}_{xy}(t)$ changes sign when the laser field strength and wave-

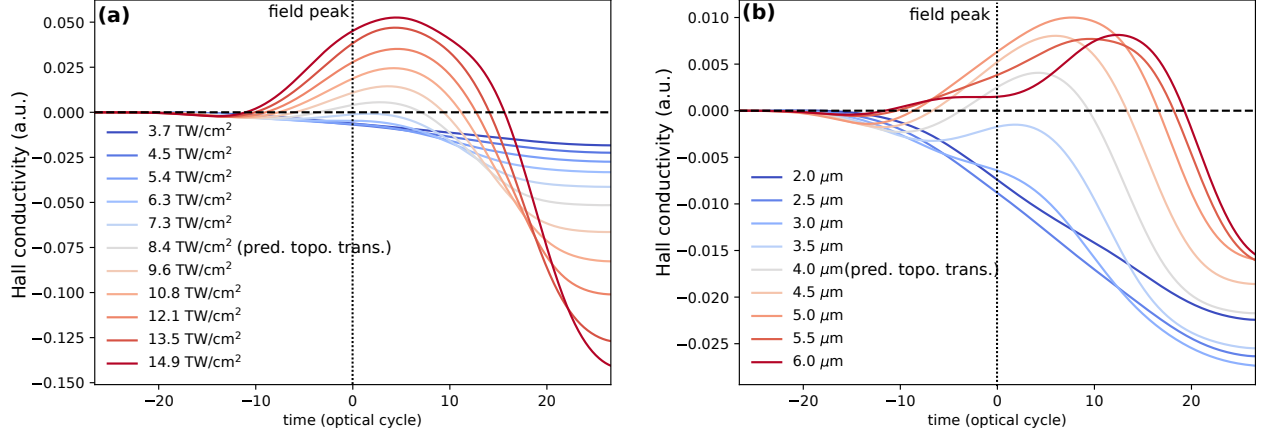


Figure 4: Light-induced topological phase transition. (a,b) Gated time-dependent anomalous Hall conductivity (AHC) in hBN, for bi-circular field with (a) different total electric field amplitude for fixed carrier $\lambda = 3\mu\text{m}$, and (b) different λ for fixed total intensity $I_{\text{tot}} = 5 \text{ TW}/\text{cm}^2$. The pulse duration is 20 cycles (FWHM), $I(\omega)/I(2\omega) = 4$, two-color delay $\varphi = 0$. The grey lines at the total intensity $I_{\text{tot}} = 8.4 \text{ TW}/\text{cm}^2$ (a) and $\lambda = 4\mu\text{m}$ (b) correspond to the analytical prediction of the topological phase transition. It coincides with the change of sign of the gated AHC close to the peak of the field (warm color lines).

length reach the parameter regime for the topological phase transition predicted by the model, both as a function of intensity and frequency (Fig. 4a,b). The sign change in $\sigma_{xy}(t)$ manifests the key feature of the topological phase transition, that is, the band gap closing and the associated change in the cycle-averaged anomalous Hall conductivity of the dressed system.

Thus, intense low-frequency fields offer unusual and robust routes for controlling electronic response in 2D materials at PHz rates. Fields with polarization states tailored to the geometry of the lattice provide the most opportunities. Controlling orientation of the field polarization relative

to the lattice controls the topological properties of the trivial dielectric by inducing and controlling complex Haldane-type second-neighbor couplings. This enables robust valley selection for multi-photon excitation. The new rules for valley selective excitation could also enable spin selectivity in materials with strong spin-orbit interaction, exploiting exponential sensitivity of strong-field excitation to the bandgap in the way similar to spin-polarization in strong-field ionization of atoms^{29,30}. Our work thus lays the grounds for a new regime of valleytronics, spintronics, and light-induced topology.

References

1. Wirth, A. *et al.* Synthesized Light Transients. *Science* **334**, 195–200 (2011).
2. Kfir, O. *et al.* Generation of bright phase-matched circularly-polarized extreme ultraviolet high harmonics. *Nature Photonics* **9**, 99 (2014). URL <https://doi.org/10.1038/nphoton.2014.293>.
3. Eckle, P. *et al.* Attosecond angular streaking. *Nature Physics* **4**, 565–570 (2008).
4. Goulielmakis, E. *et al.* Attosecond control and measurement: lightwave electronics. *Science* **317**, 769–775 (2007).
5. Krausz, F. & Ivanov, M. Attosecond physics. *Rev. Mod. Phys.* **81**, 163–234 (2009). URL <http://link.aps.org/doi/10.1103/RevModPhys.81.163>.

6. Krausz, F. & Stockman, M. I. Attosecond metrology: from electron capture to future signal processing. *Nature Photonics* **8**, 205 (2014). URL <https://doi.org/10.1038/nphoton.2014.28><http://10.0.4.14/nphoton.2014.28>.
7. Hohenleutner, M. *et al.* Real-time observation of interfering crystal electrons in high-harmonic generation. *Nature* **523**, 572 (2015). URL <https://doi.org/10.1038/nature14652><http://10.0.4.14/nature14652>.
8. Wolter, B. *et al.* Strong-Field Physics with Mid-IR Fields. *Phys. Rev. X* **5**, 21034 (2015). URL <https://link.aps.org/doi/10.1103/PhysRevX.5.021034>.
9. Schaibley, J. R. *et al.* Valleytronics in 2D materials. *Nature Reviews Materials* **1**, 16055 (2016). URL <http://dx.doi.org/10.1038/natrevmats.2016.55>.
10. Oka, T. & Aoki, H. Photovoltaic Hall effect in graphene. *Phys. Rev. B* **79**, 81406 (2009). URL <https://link.aps.org/doi/10.1103/PhysRevB.79.081406>.
11. Lindner, N. H., Refael, G. & Galitski, V. Floquet topological insulator in semiconductor quantum wells. *Nature Physics* **7**, 490 (2011). URL <https://doi.org/10.1038/nphys1926><http://10.0.4.14/nphys1926>.
12. Vitale, S. A. *et al.* Valleytronics: Opportunities, Challenges, and Paths Forward. *Small* **14**, 1801483 (2018). URL <https://doi.org/10.1002/smll.201801483>.
13. Mak, K. F., He, K., Shan, J. & Heinz, T. F. Control of valley polarization in monolayer MoS₂ by optical helicity. *Nature Nanotechnology* **7**, 494 (2012). URL <https://doi.org/10.1038/nnano.2012.96>.

14. Xiao, D., Yao, W. & Niu, Q. Valley-Contrasting Physics in Graphene: Magnetic Moment and Topological Transport. *Physical Review Letters* **99**, 236809 (2007). URL <https://link.aps.org/doi/10.1103/PhysRevLett.99.236809>.
15. Xiao, D., Liu, G.-B., Feng, W., Xu, X. & Yao, W. Coupled Spin and Valley Physics in Monolayers of MoS₂ and Other Group-VI Dichalcogenides. *Physical Review Letters* **108**, 196802 (2012). URL <https://link.aps.org/doi/10.1103/PhysRevLett.108.196802>.
16. Langer, F. *et al.* Lightwave valleytronics in a monolayer of tungsten diselenide. *Nature* **557**, 76–80 (2018). URL <https://doi.org/10.1038/s41586-018-0013-6>.
17. Ghimire, S. *et al.* Observation of high-order harmonic generation in a bulk crystal. *Nature Physics* **7**, 138 (2010). URL <https://doi.org/10.1038/nphys1847>.
18. Schiffrin, A. *et al.* Optical-field-induced current in dielectrics. *Nature* **493**, 70 (2012). URL <https://doi.org/10.1038/nature11567><http://10.0.4.14/nature11567><https://www.nature.com/articles/nature11567#supplementary-information>.
19. Garg, M. *et al.* Multi-petahertz electronic metrology. *Nature* **538** (2016). URL <http://dx.doi.org/10.1038/nature19821>.
20. Liu, H. *et al.* High-harmonic generation from an atomically thin semiconductor. *Nature Physics* **13**, 262 (2016). URL <http://dx.doi.org/10.1038/>

nphys3946<http://10.0.4.14/nphys3946>[https://www.nature.com/articles/nphys3946{#}supplementary-information](https://www.nature.com/articles/nphys3946#supplementary-information).

21. Haldane, F. D. M. Model for a Quantum Hall Effect without Landau Levels: Condensed-Matter Realization of the "Parity Anomaly". *Phys. Rev. Lett.* **61**, 2015–2018 (1988). URL <https://link.aps.org/doi/10.1103/PhysRevLett.61.2015>.
22. Dutreix, C., Stepanov, E. A. & Katsnelson, M. I. Laser-induced topological transitions in phosphorene with inversion symmetry. *Phys. Rev. B* **93**, 241404 (2016). URL <https://link.aps.org/doi/10.1103/PhysRevB.93.241404>.
23. Eichmann, H. *et al.* Polarization-dependent high-order two-color mixing. *Phys. Rev. A* **51**, R3414–R3417 (1995). URL <https://link.aps.org/doi/10.1103/PhysRevA.51.R3414>.
24. Pisanty, E. & Jiménez-Galán, Á. Strong-field approximation in a rotating frame: High-order harmonic emission from p states in bicircular fields. *Phys. Rev. A* **96**, 63401 (2017). URL <https://link.aps.org/doi/10.1103/PhysRevA.96.063401>.
25. Nag, T., Slager, R.-J., Higuchi, T. & Oka, T. Dynamical synchronization transition in interacting electron systems. *Phys. Rev. B* **100**, 134301 (2019). URL <https://link.aps.org/doi/10.1103/PhysRevB.100.134301>.
26. Tancogne-Dejean, N. & Rubio, A. Atomic-like high-harmonic generation from two-dimensional materials. *Science Advances* **4** (2018). URL <https://advances.sciencemag.org/content/4/2/eaao5207>.

27. Mak, K. F., McGill, K. L., Park, J. & McEuen, P. L. The valley Hall effect in MoS₂ transistors. *Science* **344**, 1489 (2014). URL <http://science.sciencemag.org/content/344/6191/1489.abstract>.
28. Silva, R. E. F., Jiménez-Galán, Á., Amorim, B., Smirnova, O. & Ivanov, M. Topological strong-field physics on sub-laser-cycle timescale. *Nature Photonics* (2019). URL <https://doi.org/10.1038/s41566-019-0516-1>.
29. Barth, I. & Smirnova, O. Spin-polarized electrons produced by strong-field ionization. *Physical Review A* **88**, 013401 (2013).
30. Hartung, A. *et al.* Electron spin polarization in strong-field ionization of xenon atoms. *Nature Photonics* **10**, 526 (2016).